PMT waveform modeling at the Daya Bay experiment*

Sören JETTER[1] Dan DWYER[2] JIANG Wen-Qi (蒋文奇)[1] LIU Da-Wei (刘大为)[3]
WANG Yi-Fang(王贻芳)[1] WANG Zhi-Min(王志民)[1] WEN Liang-Jian(温良剑)[1]

[1] Institute of High Energy Physics, Chinese Academy of Sciences, Beijing 100049, China
[2] California Institute of Technology, Pasadena, CA 91125, USA
[3] University of Illinois at Urbana-Champaign, Urbana, IL 61801, USA

Abstract: Detailed measurements of Hamamatsu R5912 photomultiplier signals are presented, including the single photoelectron charge response, waveform shape, nonlinearity, saturation, overshoot, oscillation, prepulsing, and afterpulsing. The results were used to build a detailed model of the PMT signal characteristics over a wide range of light intensities. Including the PMT model in simulated Daya Bay particle interactions shows no significant systematic effects that are detrimental to the experimental sensitivity.

Key words: PMT, model, simulation, Daya Bay

PACS: 29.40.Mc **DOI:** 10.1088/1674-1137/36/8/009

1 Introduction

The Daya Bay reactor experiment is designed to determine the third neutrino mixing angle θ_{13} with unprecedented precision. A sensitivity of 0.01 or better in $\sin^2 2\theta_{13}$ at 90% confidence level will be reached by measuring the relative rates and energy spectra of the antineutrinos at different distances from nuclear reactors [1].

The experimental layout of Daya Bay consists of two near and one far underground experimental halls, located 400 m and 1700 m from the reactor cores, respectively. Eight identical cylindrical detectors will be deployed to detect antineutrinos via the inverse beta-decay (IBD) reaction; two detectors at each near site and four detectors at the far site. The prompt positron signal and delayed neutron-capture signal are combined to define a neutrino event.

Each detector will have 20 metric tons of 0.1% Gadolinium-doped liquid scintillator in the innermost, antineutrino target zone. A second zone, separated from the target and outer buffer zones by transparent acrylic vessels, will be filled with undoped liquid scintillator for capturing gamma rays that escape from the target, thereby improving the antineutrino detection efficiency.

The light produced in any of the liquid-filled volumes will be detected by 192 20-cm-diameter Hamamatsu R5912 photomultiplier tubes (PMTs) that are mounted near the surface of the outermost stainless-steel cylinder.

A single 50-ohm coaxial cable is used to transmit both the high voltage to each PMT and the pulse produced at the PMT anode to the front-end electronics board. The PMTs are operated at positive voltage and the signal from the anode is capacitively coupled to ground. A signal decoupler circuit isolates the signal processing circuitry from the high voltage [2].

An energy cut of 6 MeV will be employed to select delayed neutron capture events on gadolinium. The precision of the 6 MeV threshold on the delayed energy will significantly affect the total sensitivity in $\sin^2 2\theta_{13}$. It is therefore important to understand and minimize all sources of energy biases and uncertainties associated with the PMTs. For this purpose a realistic PMT waveform model was developed. Measurements of the signal characteristics of R5912 PMTs were made to construct and tune this model. The model includes the single photoelectron charge

Received 26 September 2011, Revised 26 October 2011

* Supported by Chinese Academy of Sciences, National Natural Science Foundation of China (Project 10225524, 10475086, 10535050 and 10575056) and Ministry of Science and Technology of China

©2012 Chinese Physical Society and the Institute of High Energy Physics of the Chinese Academy of Sciences and the Institute of Modern Physics of the Chinese Academy of Sciences and IOP Publishing Ltd

response, waveform shape, nonlinearity, saturation, overshoot, baseline oscillation, prepulsing, and afterpulsing. This model was used to determine how much the PMT signal characteristics may affect the experimental sensitivity.

2 PMT measurement and modeling

To determine the details of the waveform model for the Hamamatsu tube, we studied oscilloscope traces of a number of PMT pulses, with the input charge ranging from single photoelectrons (p.e.) to saturation level. We used a blue LED and a laser diode with 405 nm wavelength as light sources to illuminate the tube. Both the light sources and the PMT were enclosed in a dark box. Averaged waveforms were sent to the oscilloscope and recorded for further analysis. The input charge of the collected traces was determined using a reference photomultiplier. To account for the charge and amplitude attenuation from the cables, we used identical 45 m cables as those employed for the Daya Bay antineutrino detectors.

2.1 Single photoelectron charge response

To analyze the single p.e. charge response with the blue LED as a light source, we used a CAMAC 2249A ADC module to integrate the PMT charge output within a 100 ns gate. The gate was triggered by the synchronization output of the LED pulse generator. Fig. 1 shows a typical charge histogram with the pedestal and the single p.e. peak.

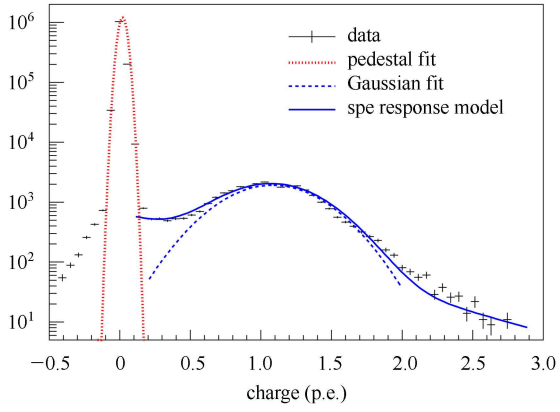

Fig. 1. Typical pedestal-subtracted single p.e. charge response at gain 3×10^7: The LED occupancy is approximately 1.5%. The single p.e. response model follows Eq. (1).

The pedestal peak around zero charge represents measurements of the fluctuating baseline when a photon was not incident upon the photocathode. In addition to the two peaks, the spectrum exhibits a non-Gaussian component around ∼0.3 p.e. To determine whether this shoulder is related to in-time detection of photons or to uncorrelated noise, we repeated the charge measurement with the same trigger settings but the LED light output disabled. As can be seen in Fig. 2, the counts outside the narrow pedestal region are virtually negligible. We thus assume the low-charge component to be an intrinsic feature of the single p.e. response. This component has been described before and has been attributed to imperfect amplification of the photoelectron from the photocathode [3, 4].

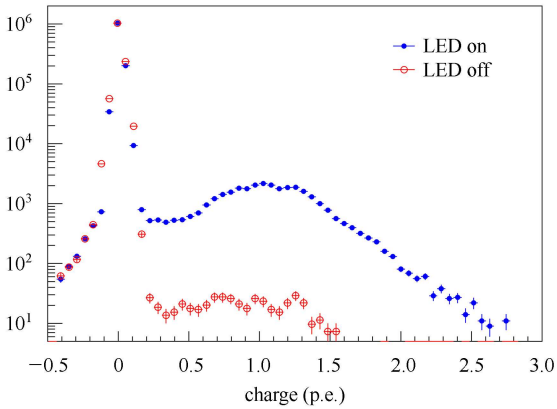

Fig. 2. Charge distribution at gain 3×10^7 with the LED turned on/off: The counts outside the narrow pedestal region are heavily suppressed.

Since the coefficient of secondary electron emission by the first dynode is on the order of 10, we can approximate the single p.e. peak by a Gaussian distribution [5]. The low-charge shoulder is parameterized using a decaying exponential with a cutoff at the right edge of the pedestal peak $q_{\rm p}$. Our full single p.e. charge response function $f(q)$ is thus:

$$f(q)=\begin{cases}(1-w)\dfrac{1}{\sigma_{\rm q}\sqrt{2\pi}}\exp\left(-\dfrac{q-q_0}{2\sigma_{\rm q}^2}\right) & \\ +w/\tau_{\rm q}\cdot\exp\left(-q/\tau_{\rm q}\right) & \text{if } q\geqslant q_{\rm p}\\ 0 & \text{if } q<q_{\rm p}\end{cases}. \quad (1)$$

The PMT gains q_0 and gain widths $\sigma_{\rm q}$ are set individually to account for the measured tube-to-tube variations on the order of 8%. The Gaussian part of the distribution corresponds to a charge resolution of ∼30%. For the non-Gaussian component we use averaged parameters for all PMTs. The typical weight w is on the order of 0.15 with a decay constant $\tau_{\rm q}\approx$ 0.5 p.e.

2.2 Single photoelectron waveform

For pulse shape analysis, we used a laser with 405 nm wavelength to illuminate the tube. A laser driver was employed to generate fast light pulses with a width of 1 ns to avoid broadening the shape of the waveforms. Fig. 3 shows a typical averaged single p.e. waveform at a gain of 2×10^7. Individual waveforms differ in amplitude but their shape is reasonably similar. A change in gain up to 5×10^7 did not significantly affect the shape, either. A gain-independent prototype waveform was thus employed for all PMTs in the simulation model. To model the asymmetric shape, we chose a log-normal equation:

$$U_{\rm peak}(t)=U^0_{\rm peak}\cdot\exp\left(-\frac{1}{2}\left(\frac{\ln(t/\tau)}{\sigma}\right)^2\right). \quad (2)$$

The function contains three free parameters: the amplitude U_0 and two parameters τ and σ, which determine the width and shape of the pulse. The amplitude U_0 is randomly computed from the single p.e. response model in Eq. (1) and the gain measured for each PMT, with 1×10^7 gain corresponding to $U^0_{\rm peak}\approx3.5$ mV.

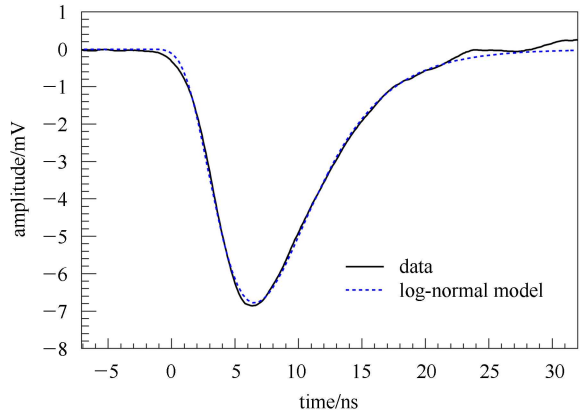

Fig. 3. Average of 500 single p.e. waveforms for one PMT at gain 2×10^7. Results for other PMTs are very similar. The waveform is well parameterized by a log-normal function.

The remaining parameters were assumed identical for all tubes. For a typical single p.e. pulse, the shaping parameters were measured at $\tau\approx7$ ns and $\sigma\approx0.45$. These numbers correspond to FWHM ≈8 ns, and a rise/fall time of 5 ns and 12 ns, respectively.

2.3 Nonlinearity and saturation

Muons passing through the antineutrino detector deposit significantly more energy than IBD events. The light seen by individual PMTs averages at ~500 p.e. and ranges to several thousand photoelectrons. However, the Hamamatsu PMT is only linear up to ~200 p.e. at gain 1×10^7. For larger numbers, both charge and amplitude show nonlinear behavior and eventually saturation sets in. The pulse shape becomes wider and more symmetric, the FWHM of waveforms associated with more than 1000 photoelectrons triples compared to single p.e. pulses. This saturation is mainly caused by space charge effects in the last dynode stages of the electron multiplier [6].

A linear model based on static single p.e. pulses for each PMT hit is thus not sufficient to render realistic waveforms for muon events. We defined the saturation factors $S_{\rm A}$ and $S_{\rm q}$ as the measured-to-ideal ratios of amplitude and charge, respectively. The saturation as a function of the input charge $N_{\rm pe}$, i.e. the number of simultaneous p.e. hits, is shown in Fig. 4. The following model [7] was found to fit the data well:

$$S_{\rm A/q}(N_{\rm pe})=\sqrt{\frac{\sqrt{1+8\left(\frac{N_{\rm pe}}{N^{\rm sat}_{\rm pe}}\right)^{\alpha}}-1}{4\left(\frac{N_{\rm pe}}{N^{\rm sat}_{\rm pe}}\right)^{\alpha}}}. \quad (3)$$

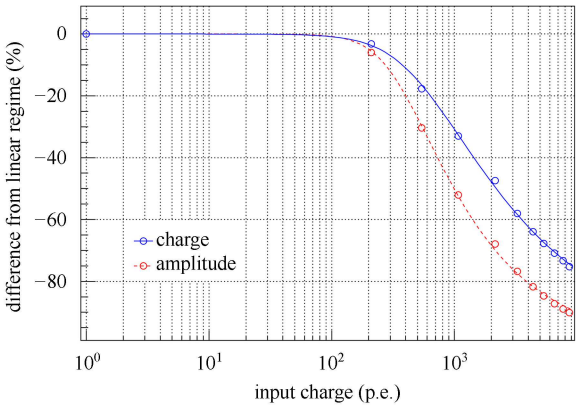

Fig. 4. Relative deviation from the ideal amplitude and charge $1-S_{\rm A/q}$ as a function of input charge $N_{\rm pe}$ at gain 1×10^7: The data were fitted using Eq. (3), which serves as the basis of the saturation model.

$N^{\rm sat}_{\rm pe}$ is the number of photoelectrons for which the saturation factor becomes $1/\sqrt{2}$, the parameter α is a real coefficient. Amplitude and charge exhibit different nonlinear behaviors: The PMT amplitude largely saturates at around 3.5 V for more than 5000 p.e., with $N^{\rm sat}_{\rm pe}\approx500$ p.e. and $\alpha\approx3$. For the charge, we find $N^{\rm sat}_{\rm pe}\approx1000$ p.e. and $\alpha\approx2$ with no indication of saturation up to 10000 photoelectrons. The amplitude saturation model is used to scale the single p.e. waveform of Eq. (2). The dependency of τ and σ on

the input charge $N_{\rm pe}$ captures the changing shape of the waveform, see Fig. 5.

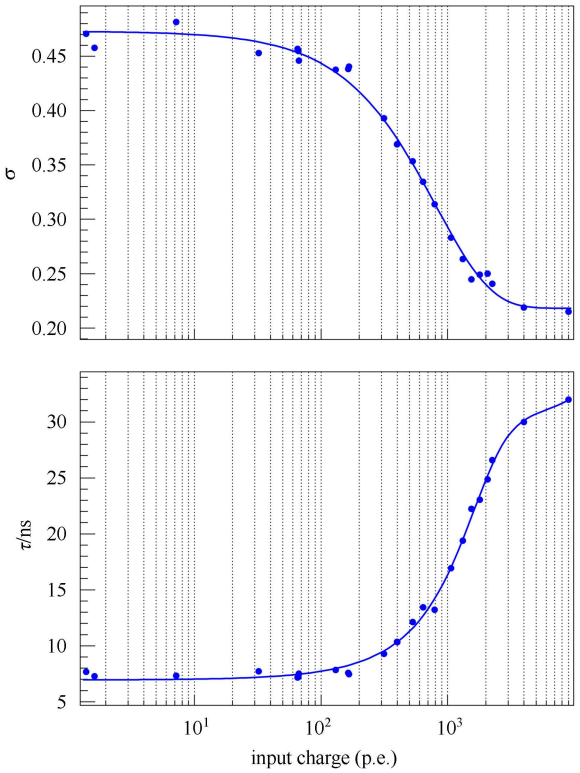

Fig. 5. The shaping parameters σ and τ as a function of input charge $N_{\rm pe}$: The left-hand plot was fitted using a double exponential function, for the right-hand plot a Fermi function was employed.

2.4 Baseline restoration

In the PMT waveform output, we observed substantial overshoot, followed by smaller periodic oscillation around the baseline. This oscillation is caused by the ceramic capacitors in the PMT base and the HV-signal decoupler [8]. The baseline shift from these overshoot and ringing effects may complicate the energy measurement and cause spurious additional triggers. Hence, in order to evaluate the impact on experimental sensitivity, the observed baseline features were incorporated into the waveform model.

We found the shape of the overshoot as shown in Fig. 6 to be fairly uniform. It was parameterized using an exponential function plus a Gaussian peak. To render the onset, the exponential is multiplied by a Fermi function:

$$U_{\rm os}(t) = U^0_{\rm os} / \left(\mathrm{e}^{\frac{50\ \rm ns - t}{10\ \rm ns}} + 1\right) \cdot \exp\left(-\frac{t}{\tau_{\rm os}}\right) + U^1_{\rm os} \cdot \exp\left(-\frac{1}{2}\left(\frac{t-t_0}{\sigma_{\rm os}}\right)^2\right). \quad (4)$$

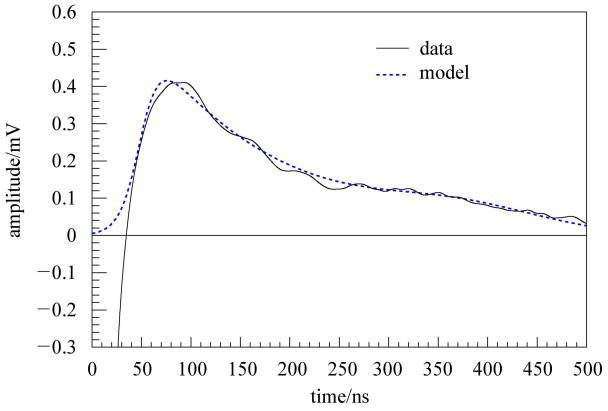

Fig. 6. The overshoot of an averaged single p.e. pulse: The shape is parameterized using a decaying exponential plus Gaussian.

Decay time $\tau_{\rm os}$ and amplitude $U^0_{\rm os}$ depend on the size of the decoupling capacitance. Larger capacitances yield smaller overshoot, however, the time to restore to the baseline increases. For the 10 nF capacitors employed in the Daya Bay decoupler circuits, the overshoot amplitude $U^0_{\rm os}$ of single p.e. pulses is in the order of 0.4 mV at gain 2×10^7, corresponding to $\sim 5\%$ of the height of the primary peak. For larger pulses, the overshoot scales with the primary charge. Since the amplitude saturates more quickly than the charge, the relative overshoot amplitude increases with input charge, exceeding 10% for large pulses, see Fig. 7. This nonlinearity is captured in the simulation by adding the charge saturation factor $S_{\rm q}$ to the otherwise static overshoot model. The decay time of the overshoot $\tau_{\rm os}$ was found to be fairly constant at ~150 ns.

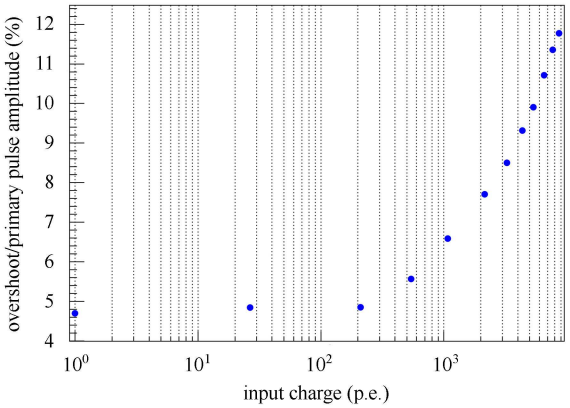

Fig. 7. Relative amplitude of the overshoot as a function of input charge at gain 2×10^7.

The temporal structure of the ringing following the overshoot can be reasonably approximated by a

harmonic oscillation with an exponential envelope:

$$U_{\rm r}(t) = U_{\rm r}^0 \cdot \exp\left(-\frac{t}{\tau_{\rm r}}\right) \cdot \cos\left(2\pi \cdot \frac{t-t_0}{T_{\rm r}}\right). \quad (5)$$

The decay time of the ringing was measured at $\tau_{\rm r} \approx 12$ μs and the oscillation period at $T_{\rm r} \approx 1.8$ μs. We estimated that the ringing, which can be in the order of several mV, would introduce unacceptable dead time to the system. In order to reduce the recovery time of the baseline, we replaced the decoupler's ceramic capacitor by a polypropylene one.

Figure 8 shows the ringing following a ∼100 p.e. primary pulse after the modification of the decoupler. The baseline oscillates quicker at $T_{\rm r} \approx 0.5$ μs and the decay time is reduced from 12 μs to less than 1 μs. This quickly decaying structure is superimposed by smaller but slower oscillations with decay time $\tau_{\rm r} \approx 2$ μs and period $T_{\rm r} \approx 4$ μs.

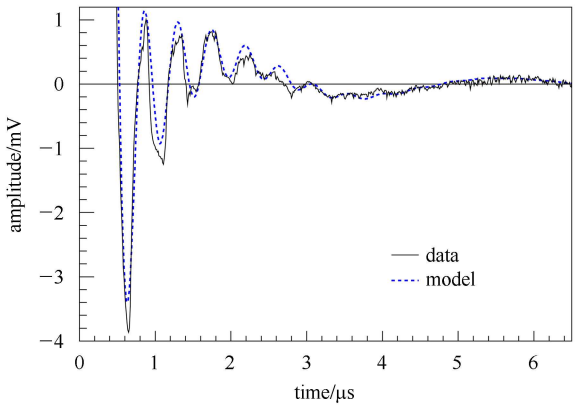

Fig. 8. Ringing from ∼100 p.e. input charge after the capacitor replacement.

The relative amplitude of the ringing was found to be ∼0.15% in the linear regime of the PMTs and continues to scale with the size of the primary peak for larger pulses. For very high input charge $\gtrsim 8000$ p.e., the baseline structure becomes irregular with significant distortion lasting up to 20 μs.

Eq. (6) shows the full parametrization of a single p.e. waveform as a function of simultaneous hits $N_{\rm pe}$, with $S_{\rm q}$ and $S_{\rm A}$ being the charge and amplitude saturation factors, respectively:

$$U(t, N_{\rm pe}) = S_{\rm A}(N_{\rm pe}) \cdot U_{\rm peak}(t, N_{\rm pe}) + S_{\rm q}(N_{\rm pe}) \cdot U_{\rm os}(t) + S_{\rm A}(N_{\rm pe}) \cdot U_{\rm r}(t). \quad (6)$$

2.5 Prepulsing and afterpulsing

Afterpulses occur some time after the initial photoelectron signal and constitute an important source of undesired background. These spurious pulses can be caused by ionized residual gas and by electrons that are backscattered to the first dynode. Since the afterpulses were found to be mostly single p.e. pulses, we employed the single p.e. charge response pdf in Eq. (1) in order to model their charge.

In order to measure the probability of a PMT hit producing a delayed pulse, we illuminated the Hamamatsu tubes with different LED intensities and counted the number of signals above threshold in a 100 ns−20 μs time interval after the primary pulse. The discriminator threshold was set to ∼0.3p.e. We used the signal count with the LED turned off to determine the dark noise background.

The measured probability as a function of the charge of the primary pulse is shown in Fig. 9. For single photoelectron pulses, the typical afterpulse ratio was measured at ∼ 1.7%. The probability scales with the charge of the primary pulse up to ∼400 p.e. and becomes nonlinear for larger pulses. For the nonlinear range, a 4th order polynomial function was employed to parameterize the data. Since we measured significant tube-to-tube variations, the afterpulse

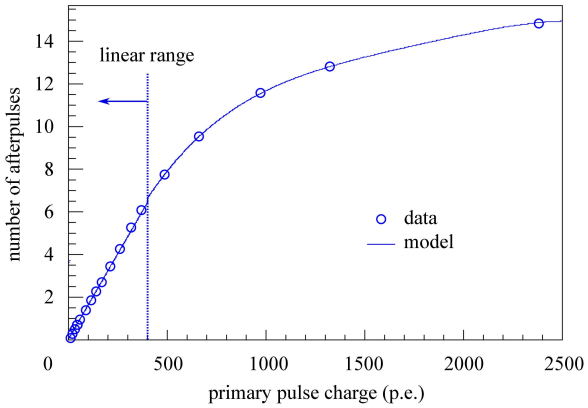

Fig. 9. Number of afterpulses as a function of primary charge after dark noise subtraction. The data were parameterized in the nonlinear range using a 4th order polynomial.

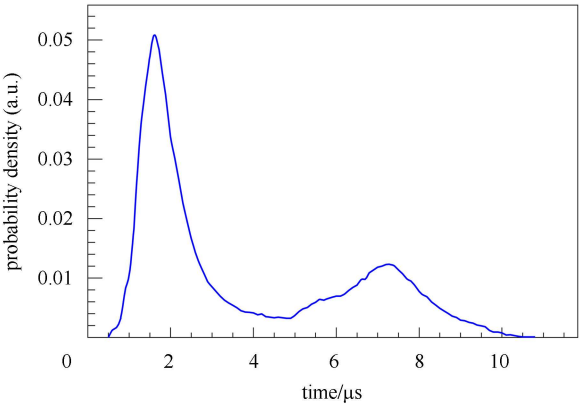

Fig. 10. Measured afterpulse time distribution.

probability in the PMT model is scaled inividually for each tube.

The timing of the afterpulsing is shown in Fig. 10. The distribution exhibits two distinctive peaks at $\sim$1.6 μs and $\sim$7 μs and is fairly uniform for all measured PMTs. The spurious pulses last for $\sim$10 μs.

Prepulses occur when photons pass the photocathod without interaction and give rise to a direct photoeffect on the surfaces of the first dynode and the focusing electrodes between the photocathode and the first dynode [4]. The prepulse rate was measured at 0.4% with tube-to-tube variations. In the PMT model, we assume a uniform time distribution within a 50 ns window before the primary pulse.

2.6 Modeling of the electronics

Figure 11 gives an overview of the PMT readout electronics. The signal from each PMT is transmitted to a single channel of a front end electronic board (FEE). In the FEE, the signal is amplified and input to a CR–$(RC)^4$ shaping circuit with a shaping time of 25 ns, which integrates the charge of the PMT signal. Two 12-bit fine and coarse range ADCs are subsequently employed to sample the shaped waveform at a speed of 40MHz, achieving a 4% charge resolution and a combined dynamic range of 1–1200 pC.

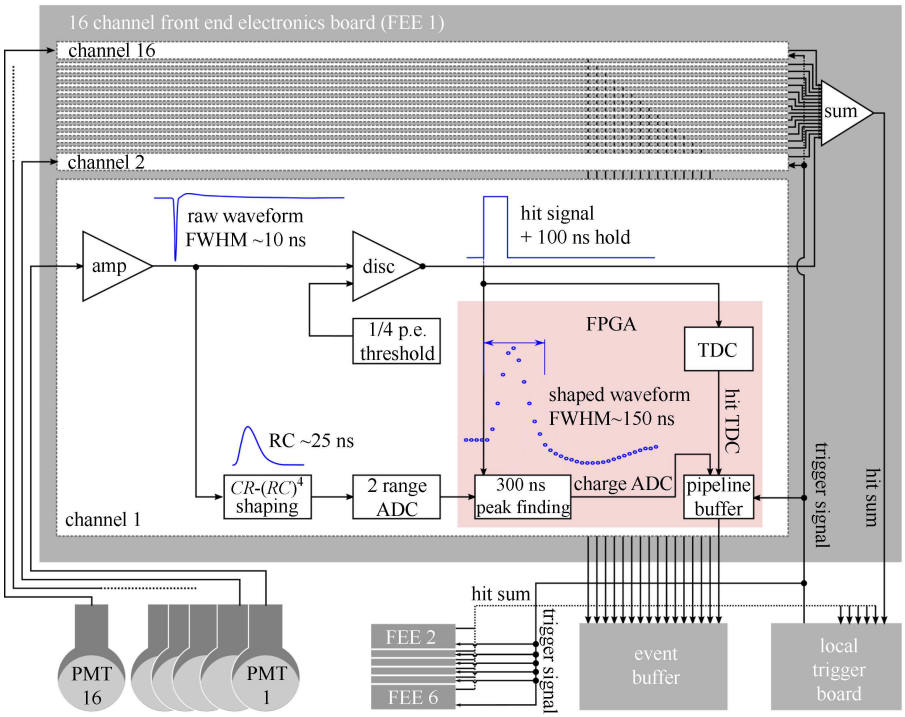

Fig. 11. Simplified scheme of the PMT electronics employed at the Daya Bay antineutrino detectors.

The amplified signal before shaping is continuously discriminated, with the threshold corresponding to ~0.25 p.e. When the signal crosses the threshold, a peak finding algorithm searches the maximum of the shaped and digitized waveform within a 300 ns time window. The peak charge value (ADC) is buffered together with the corresponding digitized threshold crossing time (TDC) in a pipeline of configurable length. In addition to the peak value, the sum of the four sampling points preceding the peak finding window is stored in order to record the possibly fluctuating PMT baseline. Should a trigger occur, the ADC/TDC pairs in all channels' pipelines will be moved to an event buffer for readout.

To generate the input for the trigger board, the digital hit signal of the respective channel will be set to 1 for 100 ns after a threshold crossing. The hit signal and the PMT signals before shaping from all channels are continuously summed in the local trigger board. The board will issue a trigger command when either the number of coincident PMT hits or the total energy signal crosses the chosen multiplicity and energy sum threshold, respectively.

The simulation model follows the electronics scheme closely to compute ADC/TDC pairs from the output of the PMT model. The generated waveforms are convolved with a CR–$(RC)^4$ response function to model the shaping circuit of the electronics. Fig. 12

shows the output of the shaping circuit after a ∼100 p.e. PMT pulse. Compared with an ideal shaping model, the circuit introduces an additional overshoot with ∼1 µs decay time. The prolonged restoration time affects the reconstructed charge of subsequent hits and was thus incorporated into the electronics model based on a double exponential function. The shaped baseline recovers below 0.01% of the primary peak within 15 µs.

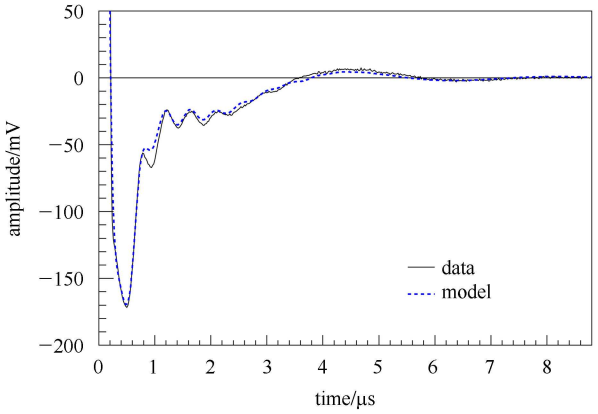

Fig. 12. PMT signal after shaping and before digitization: The example shows the baseline after a ∼100 p.e. PMT pulse.

3 Predicted effects on experimental sensitivity

There are two important uncertainties related to the observed PMT effects: The trigger dead time introduced by spurious triggers from ringing and afterpulsing and a systematic bias in the reconstructed energy of delayed events from distortions in the shaped PMT baseline. To estimate the size of these effects, a simulation was done.

To simulate the propagation of photons through the antineutrino detector, we developed a full-featured, GEANT4-based simulation suite, which we integrated into the common framework for the Daya Bay offline software. The collection of single photoelectron PMT hits generated by this suite is passed to the PMT simulation model to be converted to waveforms.

Afterpulses and prepulses are computed based on the model described above, with the afterpulse probability being a function of the input charge $N_{\rm pe}$. In the simulation, we define $N_{\rm pe}$ as the number of hits within a 20 ns time window on the same tube.

The afterpulses and prepulses are treated as single photoelectrons and are appended to the hit collection. A transit time with a Gaussian time spread is added to the hit times. For each p.e. hit, a waveform is subsequently generated, whose amplitude and shape are a function of the input charge $N_{\rm pe}$, see Eq. (6). The PMT signal is finally generated by summing all single p.e. waveforms based on their respective start time.

The simulated PMT waveforms are passed through the model of the front-end electronics, and the resulting charge and time values are examined for biases.

3.1 Spallation neutron trigger inefficiency

In IBD events, the maximum charge on individual PMTs is too small to have the subsequent baseline oscillations cross the discriminator threshold. However, the Daya Bay calibration scheme partly relies on spallation neutrons produced by cosmic muons in the antineutrino detector. Since these muons deposit large amounts of energy in the detector, the subsequent ringing will cause periodic retriggering and thus introduce substantial trigger dead time.

From a simulation based on PMT data before the modification of the decoupler, we estimate the retriggering to last longer than the mean neutron capture time on Gadolinium $\tau \approx 28$ µs. After the modification, PMT and electronics largely recover below the discriminator threshold within 5 µs, see Fig. 13.

As a consequence, the temporal structure of PMT afterpulsing becomes a decisive factor for the time cut to obtain clean calibration events. Afterpulsing occurs within a ∼10 µs time interval after a muon passage, and spurious triggering on these afterpulses may thus affect ∼25% of the spallation neutron events.

The expected effective trigger dead times and inefficiencies from the observed PMT effects are summarized in Table 1.

Table 1. Expected effective trigger dead times after muons events and resulting inefficiency of spallation neutron selection.

	spallation n selection	
	dead time/µs	inefficiency (%)
from ringing (old dec.)	>30	>60
from ringing (new dec.)	~ 5	~ 15
from afterpulsing	~ 10	~ 25

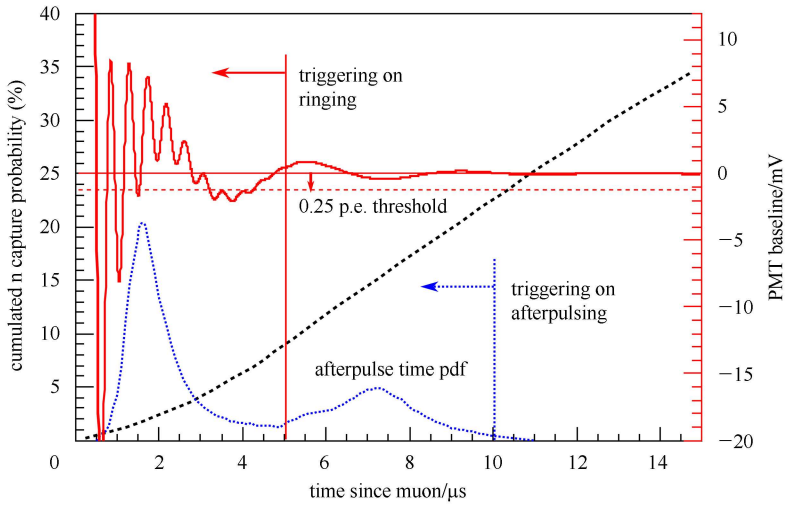

Fig. 13. Illustration of the PMT response to a min. ionizing muon. The example baseline corresponds to a ∼1000 p.e. primary pulse.

3.2 Energy uncertainty

Even when the unshaped PMT signal has restored well below the discriminator threshold, the shaped baseline still exhibits significant distortion. This bias may compromise the precision of the measurement of both the energy of spallation neutrons after muons and the delayed energy of inverse beta-decays.

As discussed, the trigger system recovers within ∼10 μs after a muon passes through the detector. At later times, the baseline distortion may continue to bias the measurement of energy of spallation neutron captures. Our charge calibration algorithm partly suppresses this bias by making use of the dynamic pedestal data recorded with each PMT hit.

For neutrons following minimum-ionizing muons, simulation indicates an energy distortion on the order of 1% for 11–16 μs and no bias for longer capture times. Larger distortions lasting ∼ 20 μs are expected after muon-induced particle showers, which can generate more than 10000 hits on each PMT. An estimated ∼ 60% of all spallation neutrons will thus remain unaffected in their reconstructed energy by the system recovery after large light yield.

Positron annihilation events typically only deposit 1–2 p.e. per PMT, the baseline fully recovers within ∼6 μs. We thus expect ∼15% of the delayed IBD events to be lightly biased in energy. This bias may affect the uncertainty $\sigma_{\epsilon_{\rm E}}$ associated with the 6 MeV energy cut employed on the delayed energy distribution, which is crucial for the total sensitivity of our experiment. To quantify this effect, we generated two samples of 500 k inverse beta decay events, uniformly distributed in the antineutrino target zone, with the baseline restoration model turned on and off. The resulting neutron capture energy distributions are shown in Fig. 14.

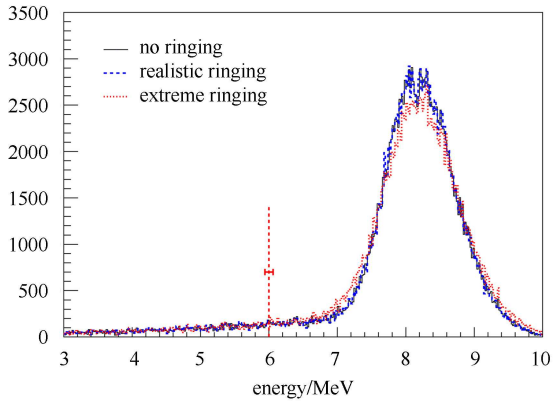

Fig. 14. Reconstructed energy distribution of neutron capture events: A 1% variation of the 6 MeV selection cut is applied to estimate its uncertainty.

We computed the uncertainty of the neutron selection by a 1% variation of the energy cut. To reduce statistical errors, the slope around the energy cut was fitted by an exponential function to calculate the efficiencies of the shifted cuts.

The additional smearing in the reconstructed delayed energy introduced by the ringing was computed at 0.5% and 0.3% for the old and new decoupler circuit, respectively. Efficiency $\epsilon_{\rm E}$ and uncertainty $\sigma_{\epsilon_{\rm E}}$ of the neutron selection remain unaffected. This is expected since the loss in energy resolution is small and the inefficiency of the delayed energy cut is primarily determined by the fraction of gammas escaping the scintillator zones. To check on a more extreme scenario, we raised the amplitude of the ringing by

a factor of 5. Only then a slight degradation in efficiency and uncertainty was found, see Table 2.

Table 2. Expected efficiency and uncertainty of the IBD delayed neutron selection for an ideal PMT baseline and the oscillation measured before and after the modification of the decoupler (dec.).

	IBD n selection	
	efficiency ϵ_{E} (%)	uncertainty $\sigma_{\epsilon_{\mathrm{E}}}$ (%)
ideal baseline	92.55	0.194±0.005
ringing (old dec.)	92.54	0.194±0.005
ringing (new dec.)	92.55	0.194±0.005
ringing (5×)	92.28	0.208±0.005

4 Conclusion

A realistic modeling of the analog PMT response was achieved by analysis of waveforms collected at a PMT test stand. A log-normal function was found to parameterize the waveforms quite well. Nonlinear features, baseline restoration, afterpulsing, prepulsing, and electronics effects were included in the model. The model reproduces individual PMT waveforms within a few percent error and provides a powerful tool to evaluate the impact of characteristics of the PMTs and the electronics on experimental uncertainties via Monte Carlo studies. Based on this model, we found that the observed ringing would not affect our energy sensitivity but might introduce unacceptable trigger dead time. This issue was resolved by modification of the HV decoupler.

We do not expect the PMT and electronics features in the improved system to have any significant impact on the sensitivity of the Daya Bay experiment, in particular on the uncertainty associated with the delayed energy threshold to select neutrino candidates and the use of spallation neutrons to monitor the detector response.

This study could not have proceeded without the support of the Daya Bay collaboration as a whole. We would particularly like to thank the PMT Group for their valuable support.

References

1 GUO X et al. (Daya-Bay collaboration). arXiv:hep-ex/0701029
2 LIU D. PMT Evaluation for the Daya Bay Neutrino Experiment, Nuclear Science Symposium Conference Record, 2008. NSS '08. IEEE, 3133–3139
3 Dossi R, Ianni A, Ranucci G, Smirnov O Y. Nucl. Instrum. Methods A, 2000, **451**: 623
4 Coates P B. J. Phys. D: Appl. Phys., 1973, **6**: 153
5 Bellamy E H et al. (SDC collaboration). Nucl. Instrum. Methods A, 1994, **339**: 468–476
6 Photomultiplier Tubes: Basics and Applications. Third Edition. Hamamatsu, 2006
7 Zbiri K. Simplified PMT Model. arXiv:0809.4210 [physics.ins-det]
8 JIANG W, GU S, Joseph J, LIU D et al. Chin. Phys. C (HEP & NP), 2012, **36**(3): 235